

Simulations of the Modular Axisymmetric Scramjet Test Rig Under Reacting Flow Conditions

Jacob J. Lampenfield,[†]Tomasz G. Drozda,[‡]Matthew O'Connell,[‡]
NASA Langley Research Center, Hampton, VA 23681

and

Timothy M. Ombrello,[§]
AFRL, WPAFB, OH 45433

ABSTRACT

Simulations of the Air Force Research Laboratory (AFRL) Modular Axisymmetric Scramjet Test Rig (MASTeR) are presented. MASTeR is a parametric test article capable of investigating various scramjet cavity flameholder designs and fueling strategies with the goal to characterize and optimize flameholding capability. In the current work, three cavity aspect ratios, and two fueling strategies (upstream and in-cavity) with ethylene at a nominal facility pressure and temperature condition are evaluated. The reacting simulations are performed, and the resulting flow characteristics are discussed. For each configuration and fueling strategy, cavity residence time, entrainment rate, and fuel-air equivalence ratio are computed. The MASTeR geometry is defined in Engineering Sketch Pad (ESP) and the simulations use a sketch-to-solution (S2S) automated unstructured grid adaptation tool in VULCAN-CFD. This tool automatically generates a simulation grid from the ESP geometry and systematically adapts it to the numerical solution based on the Hessian error estimate of a specified flow field parameter. Reynolds averaged simulations (RAS) are used with a two-equation linear eddy viscosity and diffusivity model. The resulting database can be compared with the experimental data as those become available, and explored to develop models for cavity performance for scramjet propulsion design applications.

Statement A: Approved for public release; distribution is unlimited.

[†]Research Engineer, Analytical Mechanics Associates, Inc.

[‡]Research Scientist, Hypersonic Airbreathing Propulsion Branch.

[§]Senior Research Aerospace Engineer, High Speed Systems

INTRODUCTION

Supersonic combustion ramjet (Scramjet) powerhead designs, leading to efficient fuel-air mixing, flameholding, and combustion remain one of the key challenges in scramjet flowpath design. Even if fuel and air are mixed optimally, the high-speed flow requires that chemical reactions occur over a millisecond or less. To reduce the ignition time in scramjets and support robust and stable combustion, flameholder devices are typically employed.¹⁻³ These flameholding devices often require the use of geometric features that produce a region that is sheltered from the high-speed flow. For example, the aerodynamic wakes of strut fuel injectors can serve as flameholders; however, one non-intrusive option is a recessed cavity. Cavity flameholders are quite common and allow a fraction of freestream fuel and air to be entrained into the cavity by mass exchange across the shear layer that separates the cavity from the freestream. Inside the cavity, the slow recirculating flow increases the residence time and allows the entrained fuel and air to chemically react. The resulting hot combustion products and radicals subsequently diffuse out of the cavity and into the freestream through the cavity shear layer. Once out of the cavity, the hot combustion products mix with the fuel and air in the freestream to significantly reduce the ignition delay time of the resulting mixture. This facilitates rapid combustion and maintains combustion across a wide range of operating conditions, which is required for efficient scramjet operation.

The design details of the cavity and fueling strategy are a subject of ongoing research.^{4,5} To that end, the Modular Axisymmetric Scramjet Test Rig (MASTeR)⁶ is a new 1X-scale axisymmetric combustor, with 9 different cavity sizes, consisting of three sets of cavity depths, and three different lengths. The airflow is provided by a Mach 2 or Mach 3 facility nozzle with an equivalent flight enthalpy up to 1000°F. The combustor is designed to use gaseous fuels such as ethylene, methane/ethylene mix, and propane with fuel injected upstream of and directly into the cavity flameholder. The experimental rig is expected to be tested in Research Cell 19 at AFRL over the next couple of years.

The current work explores the experimental space using reacting Reynolds-averaged simulations (RAS) to provide an understanding about the MASTeR operating performance. Of particular interest are the isolator shock train location and equivalence ratio (ER) in the cavity, which will be measured. For yet unknown limits of lean and rich conditions, a diminished or extinguished cavity flameholder operation is expected.

GEOMETRY AND SIMULATED FLOW CONDITIONS

MASTeR is an axisymmetric modular test article designed to evaluate flameholding capabilities of cavities of various geometries. MASTeR consists of a Mach 2 or 3 facility nozzle, 31.272 inch-long isolator, 7.818 inch-long powerhead section, variable depth and length cavity flameholder, and 22 inch-long combustor. The isolator has an expansion half-angle of about 0.35 degrees. The powerhead section has an expansion half-angle of about 1.25 degrees. It also includes 32 circumferential wall-normal primary fuel injectors, each with a diameter of 0.05 inches and located 4.327 inches downstream of the isolator. The cavity design supports three length-to-depth ratios (L/D) of 4, 6, and 8, and three depths (D) of 0.25, 0.75, and 1.25 inches. The length of the cavity (L) is a product of L/D and D and is measured from the backward facing step to the midpoint of the downstream cavity closeout face, which is angled at 22.5 degrees. The cavity can be fueled directly via 16 circumferential wall-normal secondary fuel injectors, each with a diameter of 0.05 inches and located on the cavity backward-facing face at a mid-cavity depth for the cavity with a depth of 1.25 inches and closer to the cavity floor for the cavity with a depth of 0.75 inches. However, the cavity with a depth of 0.25 inches does not include secondary cavity injection. Downstream of the cavity, the combustor section has an expansion half-angle of 1.25 degrees. Figure 1 shows a schematic of the MASTeR test article for L/D=6 and D=0.75 inches with various elements annotated.

The air flow corresponds to a total pressure and total temperature of 50.0 psi and 600°F, respectively, and is expanded through the facility nozzle to a Mach number of about 2. A thermally perfect mixture of 21%

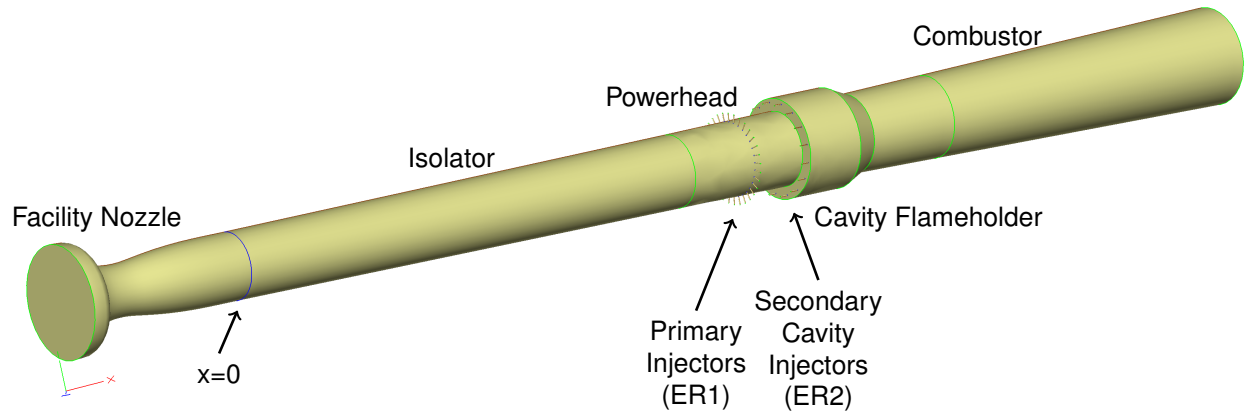


Figure 1. Schematic of the MASTeR test article for L/D=6 and D=0.75 inches.

oxygen and 79% nitrogen by mole was used for the air. The test article is fueled with ethylene with a total temperature of 80°F from both primary and secondary injectors. In the current work, the mass flow rate of ethylene was set as a fraction of the global ER and varied in the range of 0.04–0.4 for the primary injectors and 0.02–0.2 for the secondary injectors. The ethylene flow through the injectors was choked for most of these ranges; however, subsonic (unchoked) conditions resulted at the lower values of the ERs.

A Latin hypercube sampling (LHS) method was used to generate a design-space-filling list of cases to simulate. The independent variables for the current work were the primary injector ER (ER1), the secondary injector ER (ER2), and L/D, with D equal to 0.75 inches. A total of 45 cases were simulated, 15 for each L/D. A scatter plot of the simulated ERs, colored by L/D value, is shown in Fig. 2. The colors green, blue, and magenta denote the L/D values of 4, 6, and 8, respectively.

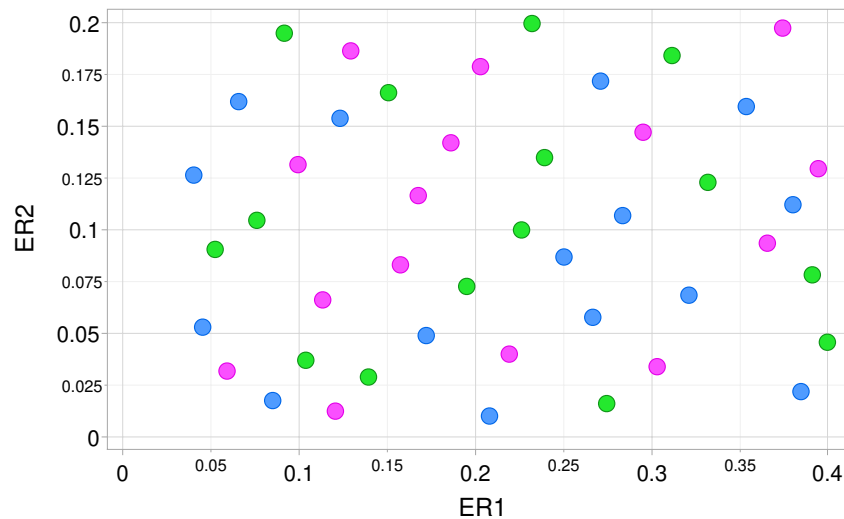


Figure 2. Scatter plot of ER1 vs ER2 for all simulated cases. Colors green, blue, and magenta denote L/D values of 4, 6, and 8, respectively.

METRICS OF INTEREST

A number of different metrics for mixing and combustion efficiency, thermodynamic losses, and performance exist with a rigorous analysis proposed by Riggins et al.⁷ For the current study, the following were chosen: mixing efficiency based on stoichiometric proportions of fuel and air, and combustion efficiency based on fuel depletion. The mixing efficiency is defined following Mao et al.:⁸

$$\eta_m = \frac{\int \alpha_R \rho u dA}{\int \alpha \rho u dA} \quad (1)$$

where the integration is over a single streamwise, constant cross-stream plane (x-plane) of interest, and α is the fuel or oxidizer mass fraction depending on whether the global ER is less than or greater than 1, respectively. The quantity α_R is defined as the amount of fuel or oxidizer that would react if complete reaction took place without further mixing, i.e.,

$$\alpha_R = \begin{cases} \alpha, & \alpha \leq \alpha_{st} \\ \frac{\alpha_{st}}{1-\alpha_{st}}(1-\alpha), & \alpha > \alpha_{st} \end{cases} \quad (2)$$

where α_{st} is the stoichiometric value of fuel or oxidizer mass fraction. For cases with overall ER of one, either fuel or oxidizer can be used in place of α . However, choosing the fuel has a minor benefit of clarifying somewhat the meaning of Eq. (2), which becomes

$$\alpha_R = \begin{cases} Y_f, & Y_f \leq Y_{f,st} \\ FAR_{st} Y_a, & Y_f > Y_{f,st} \end{cases} \quad (3)$$

where Y denotes mass fraction, and subscripts f and a denote fuel and air streams, respectively. The quantity FAR_{st} denotes the stoichiometric value of the fuel-to-air ratio and equals to 0.068 for ethylene-air mixtures. It is clear from the above equation that if the local value of the mass fraction of fuel is less than its stoichiometric value, then that amount is ‘‘counted’’ as fully mixed because there is a sufficient amount of air to potentially deplete all of the fuel if reactions were allowed. However, when the local value of the fuel mass fraction is greater than its stoichiometric value, then the only part that could react is that which is in stoichiometric proportion to the local value of the mass fraction of the air. Therefore, only that portion is counted as being mixed in Eq. (1). The mixing efficiency formula of Mao et al.⁸ can also be used to analyze mixing in the reacting simulations; however, since fuel and oxidizer are consumed to make combustion products, care must be taken to use the elemental mass fractions of either fuel or oxidizer (i.e., mass fractions of all elements that originate in either fuel or oxidizer streams).

The combustion efficiency quantifies how completely a given flowpath is able to process a mixture of fuel and air into combustion products, thereby enabling heat release into the flow. There exists a number of combustion efficiency definitions that include combinations of the total temperature, the enthalpy or enthalpy of formation as a function of the local equilibrium composition, and the fuel/oxidizer depletion or combustion product formation.⁹ In this work, the simplest definition based on the fuel mass depletion is used, i.e.,

$$\eta_c = 1 - \frac{\dot{m}_f}{\dot{m}_{f,tot}} \quad (4)$$

where \dot{m}_f and $\dot{m}_{f,tot}$ are the integrated mass flow rates of fuel at a streamwise location of interest and the total injected fuel flow rate, respectively. For mixing-only simulations, the above quantity is identically zero, whereas for reacting simulations, its value increases monotonically to one when all of the fuel has been depleted. For fuel-rich simulations, the formulation based on the oxidizer mass fraction depletion would be appropriate.

Another metric of interest which characterizes overall combustor operation as well as the cavity flameholder state is the ER. ER can be computed for the entire combustor, where a value of one identifies stoichiometric proportions of fuel and air. But, ER can also be evaluated locally to help identify the local mixture state.

Table 1. Elemental mixture fraction weights.

γ_C	γ_H	γ_O	Notes
$\frac{2}{W_C}$	$\frac{1}{2W_H}$	$-\frac{1}{W_O}$	Bilger's Definition
$\frac{2}{W_C}$	$\frac{1}{2W_H}$	0	Barlow's Definition (for Sandia Flames)
1	0	0	Elemental mixture fraction for C
0	1	0	Elemental mixture fraction for H

ER values of less than one indicate excess air, that is fuel "lean" state, whereas values greater than one identify excess fuel and therefore fuel "rich" conditions. Excessively lean or rich conditions do not support combustion. In addition, certain ranges of lean conditions can lead to combustion instabilities. For cavity flameholders in scramjets, stoichiometric or slightly rich operation is generally preferred, however, this may be difficult to maintain across a range of flow conditions expected in flight. Therefore, understanding the operational envelope of a cavity flameholder is of importance.

A convenient way to compute the ER is by using the mixture fraction. The mixture fraction represents a mass fraction of all material that originated in the fuel stream that is present locally in the mixture. The formal definition of the mixture fraction can be written as:

$$f = \frac{\beta - \beta_O}{\beta_F - \beta_O} \quad (5)$$

where f is the mixture fraction and β_F and β_O are the mass fractions of the fuel material in the fuel and oxidizer streams, respectively. The definition of β is:

$$\beta = \sum_i \gamma_i f_i = \sum_i \gamma_i \sum_j \frac{a_{ij} W_i Y_j}{W_j} \quad (6)$$

where γ_i is a weight corresponding to each element (i.e., C, H, O) present in the mixture, f_i is elemental mass fractions (i.e., f_C , f_H , f_O), a_{ij} is the number of atoms of i in species j , Y and W are the mass fractions and molecular weights of species in the gas mixture, respectively. It is clear from Eq. (6) that mixture fraction is a linear combination of elemental mass fractions. By conservation of mass, the latter are conserved scalars. The values of γ define a particular mixture fraction. Table 1 shows the several typically used definitions among which Barlow's definition is commonly used in turbulent combustion.

The mixture fraction can be used to calculate fuel-to-oxidizer ratio. Since by definition, the mixture fraction represents the mass fraction of elements originating in the fuel stream, the fuel-to-oxidizer ratio becomes:

$$\frac{F}{O} = \frac{f}{1 - f} \quad (7)$$

where $1 - f$ is the mass fraction of material in the mixture that originated in the oxidizer stream. When the oxidizer is air, Eq. (7) represents fuel-to-air ratio.

Finally, the ER can be computed from mixture fraction. By definition the ER is:

$$ER = \frac{F/O}{(F/O)_{st}} = \frac{1 - f_{st}}{f_{st}} \frac{f}{1 - f} \quad (8)$$

where subscript st denotes the value at stoichiometry. The stoichiometric value of ethylene mixture fraction is 0.0637, and can be readily computed for other fuels.

For the current work, ER is evaluated at several locations in the cavity. Figure 3 shows a schematic of a cavity flameholder with the probe locations denoted by circles. For all cavities, two fixed locations 0.1 inches from the cavity floor, and 0.5 and 1.5 inches from the cavity backface are used. In addition, three other locations at half-cavity-depth ($D/2$) and $L/4$, $L/2$, and $3/4L$ are used. These locations help characterize the extent of variation of flow properties in the cavity.

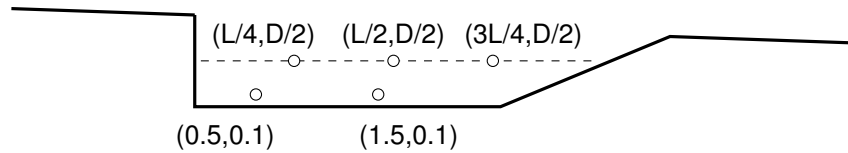


Figure 3. Schematic of the cavity flameholder with various probe locations denoted by circles.

UNSTRUCTURED GRID ADAPTION METHODOLOGY

The overall process of anisotropic grid adaptation with the VULCAN-CFD code¹⁰ for aerodynamic problems, and the methodology behind the adaptation tool, were previously outlined by Kleb et al.¹¹ and O'Connell et al.¹² The current work discusses the application of these methods to this high-speed reacting case. The first step required for using the adaptive grid tool involves creating a solid model of the problem domain geometry using Engineering Sketch Pad (ESP).¹³ Figure 4 shows the geometric progression of constructing the test article in ESP. The first step in creating the geometry was to generate a sketch of the nozzle by creating a line segment and splining together nozzle point coordinates, resulting in a closed sketch. This sketch was then rotated 360 degrees to generate a 3D body of the facility nozzle. The next step was to generate a sketch of the isolator, powerhead, cavity and combustor by creating line segments from the specified points of the geometry. The closed sketch was rotated 360 degrees to create a 3D body. One upstream fuel port and cavity fuel port were generated in the same manner as the previous bodies. A pattern was then used to create the remaining fuel ports by specifying the total number of injectors, translating each injector to the correct position, and rotating the injector so that the injection angle is normal to the flow. The smallest symmetric sector is then defined, and the unneeded portion of the geometry is subtracted, resulting in the pie slice shown in the bottom image of Fig. 4. Although there is a ring of primary and secondary injectors, the pie slice only contains a half primary injector on each symmetry plane and a half secondary injector on one symmetry plane. Once a script for generating a solid model has been created, the geometry is parametric and can be easily modified. Although not used for this work, this capability can be used for optimization purposes.

Once the geometry has been created and the boundary faces have been identified, an initial surface triangulation is created by the Electronic Geometry Aircraft Design System (EGADS).¹⁴ The surface grid associates each triangular element with the underlying geometric entities, which establishes a grid-to-geometry association. Establishing and maintaining this association during the entire adaptation process is important because it is used by the grid adaptation tool, *refine*,¹⁵ to ensure each new grid remains representative of the true geometry during grid adaptation. Finally, TetGen¹⁶ is used to create the initial volume grid.

After the initial volume grid has been generated, VULCAN-CFD is used to obtain the first solution. All future adaptations are generated based on the stride, complexity multiplier, and sensor field variable specified by the user in the adaptation input file. In the context of grid adaptation, complexity level is proportional to the total grid count in a mesh. The stride indicates the number of times to perform a simulation with a certain complexity level before increasing the number of grid cells. The complexity multiplier represents the factor that the grid complexity is multiplied by between complexity levels. Thus, grids at the same complexity level exhibit about the same number of grid cells to within a few percent, and those with higher complexity levels exhibit a proportionally larger number of grid cells. The sensor field variable is the flowfield variable in which error is estimated to decide where to place grid cells. In the current case, Mach number is used as the sensor field variable. After each new grid is created, VULCAN-CFD is used to obtain a solution, the next grid is created, and the current solution is interpolated onto the new grid and used as an initial condition for the next VULCAN-CFD simulation. This adaptation loop continues until grid convergence of the metric of interest is reached. A visual representation of this entire process is shown schematically in Fig. 5. For more details, refer to O'Connell et al.¹² The first stage in the adaption strategy involved using only first-

order numerics for the early simulations (adaptations 1–3), with each simulation only partially converged, in order to rapidly drive the grid refinement toward approximate locations in the flow where it is needed. The philosophy behind this approach was to generate a high-quality initial condition from which the final few fully converged simulations would be run. For these early adaptations, the stride was set to 2 and the complexity multiplier was set to 2. This means that after two adaptation iterations the grid complexity was increased by a factor of 2, thus, increasing the grid cell count. Within the same stride (indicating grids at the same complexity level), grid cells are repositioned rather than added. So, with these settings, grid cells are repositioned once between refinements based on the flow features. An ignition sub-domain was used in this stage to establish ignition of the fuel and ensure reactions occur. At the end of this stage, the key features of the flow should be highlighted via presence of the grid clustering around them.

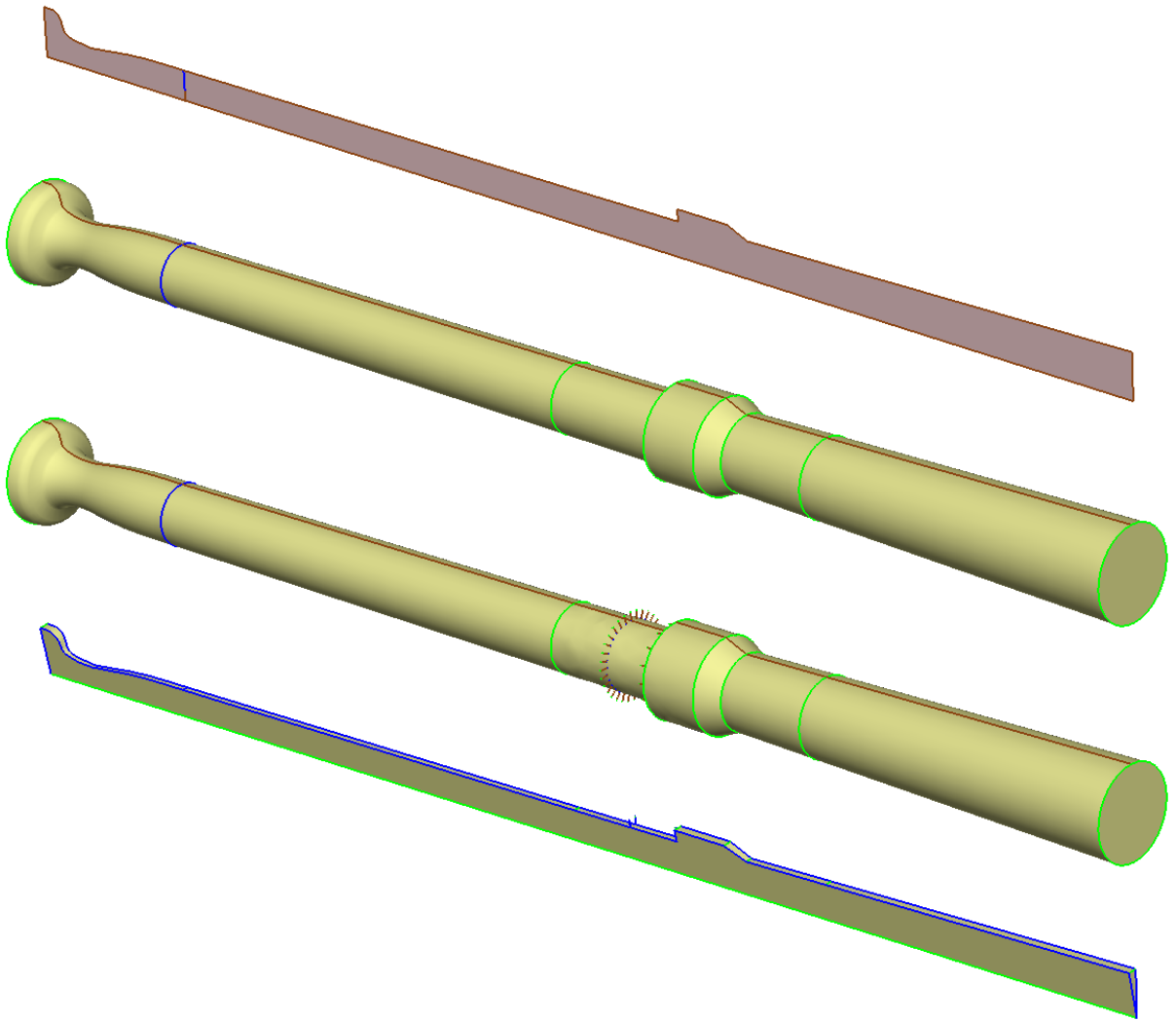


Figure 4. Graphical steps taken in the ESP script to construct the MASTeR test article (from top-to-bottom): closed sketch of the MASTeR geometry, sketch rotated 360 degrees, MASTeR with primary and secondary injectors, and smallest symmetric sector for simulations.

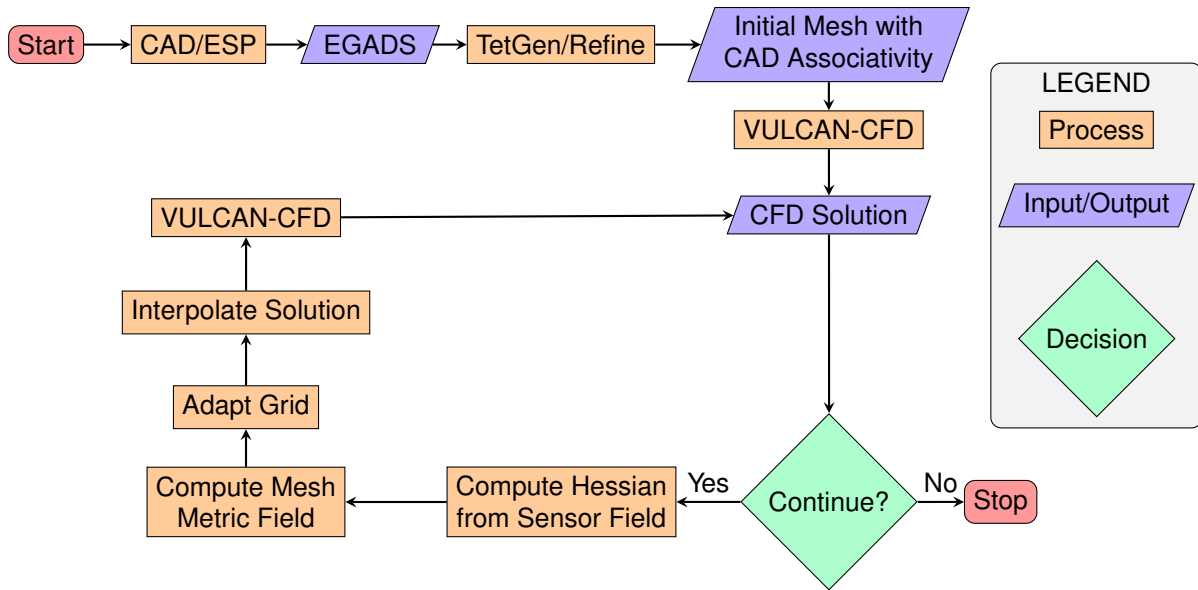


Figure 5. Adaptation workflow: An initial grid is iteratively adapted to control interpolation error in the Mach number field.

Once the grid has been adapted to obtain bulk flow features and establish preliminary refinement, the second stage involved continuing the adaptation process using only second-order numerics in order to further refine flow features and drive the simulation toward an even more accurate initial condition for the final adaptations while simultaneously adding grid points to improve the flow feature resolution. This stage was carried out for adaptations 4–5, with the stride and multiplier settings remaining the same as used in the first stage of the simulation process. The number of iterations used for each simulation in this stage remained the same as before, with these simulations also only partially converged. The ignition sub-domain was still used in this stage because for some cases the reactions were not well established, which caused cavity flame out. The final second-order solutions were used to adapt the next grid. The final stage, which was carried out for adaptations 6–10, was performed without an ignition sub-domain as the reactions are well established and no longer need an ignition source. The resulting cell counts are shown in Table 2. The values in this table reflect the number of grid cells for the entire computational domain.

Table 2. Number of grid cells used in the current simulations.

Adaptation	Grid Cells
1	121,135
4	240,652
6	485,260
8	936,533
10	1,892,995

NUMERICAL METHOD

The numerical simulations were performed using the VULCAN-CFD code. VULCAN-CFD is a cell-centered finite-volume solver widely used for high-speed flow simulations. For this work, RAS were performed. The advective terms were computed using the Monotone Upstream-Centered Scheme for Conservation

Laws (MUSCL)¹⁷ with the Low-Dissipation Flux-Split Scheme (LDFSS) of Edwards.¹⁸ The thermodynamic properties of the mixture components were computed using the curve fits of McBride et al.¹⁹ The governing equations were integrated using the symmetric Gauss-Seidel (SGS)²⁰ method.

The Menter-BSL²¹ turbulence model was used in the current work. The Reynolds heat flux and species mass flux were modeled using a gradient diffusion model with turbulent Prandtl number (Pr_t) and Schmidt number (Sc_t) of 0.9 and 0.5, respectively. Wilcox wall matching functions²² were also used; however, their implementation in VULCAN-CFD includes a modification that allows the simulations to recover the integrate-to-the-wall behavior as the value of normalized wall-distance, y^+ , approaches one. The simulations were converged until the total integrated mass flow rate and the total integrated heat flux on the walls remained constant to at least 4 decimal places.

The grid convergence with respect to the metric of interest is arrived at automatically for the adaptive grid approach due to the nature of the adaptation process as long as the selected adaptation sensor field is sufficiently sensitive to that metric. For the current work, the mixing efficiency is used as the metric of interest and the Mach number is selected as the sensor field. The Mach number is a reasonable choice for the sensor field because it exhibits sensitivity to not only compressible flow features but also mixture composition variations and combustion. Local flow entropy also satisfies these criteria and could have been used instead of the Mach number. Nevertheless, when using the Mach number sensor field, the adaptation adds grid cells in the vicinity of shocks, as well as, mixing and reaction gradients, thereby naturally improving the resolution of these flow features until little change can be observed in the metric of interest that is used to determine the grid convergence.

The inflow of the facility nozzle and the fuel port inflow domains utilized a subsonic inflow boundary condition with the mass flux, total temperature and gas species specified. The outflow of the domain utilized a subsonic outflow boundary condition with the static pressure specified as the simulations were performed to model a mechanically back-pressured experimental configuration. No-slip, thermally coupled fluid/surface wall boundary conditions were used for the facility nozzle, isolator, powerhead, cavity, combustor, and nozzle walls. A slip wall boundary condition was used for the fuel port walls. The values of y^+ on the final grids for the unstructured runs for were found to be no greater than 37 and an average value across all cases of 21.6.

Chemical reactions were modeled using the 6-species, 3-reaction reduced chemical kinetics model shown in Table 3. The forward and backward reaction rate constants follow an Arrhenius temperature dependence and an equilibrium assumption, respectively. A turbulence-chemistry interaction model was not used. For this chemical reaction mechanism, the mixture fraction with Barlow's coefficients from Table 1 and Eqs. (5) and (6), for ethylene becomes:

$$f = Y_{C_2H_4} + \frac{W_{C_2H_4}}{6} \left(\frac{2Y_{CO_2}}{W_{CO_2}} + \frac{Y_{H_2O}}{W_{H_2O}} + \frac{2Y_{CO}}{W_{CO}} + \frac{Y_{H_2}}{W_{H_2}} \right) \quad (9)$$

Table 3. 6-species, 3-reaction reduced chemical kinetics model for ethylene used in the current work.

#	Reaction*		
1	$C_2H_4 + O_2 \leftrightarrow 2CO + 2H_2$		
2	$2CO + O_2 \leftrightarrow CO_2 + CO_2$		
3	$2H_2 + O_2 \leftrightarrow H_2O + H_2O$		
#	A	B	Ta (K)
1	2.10E14	0.0	18015.30
2	2.48E14	2.0	10134.86
3	3.00E23	-1.0	0.00

*Forward reaction rate constant: $k_1^f = A_1 T^{B_1} \exp\left(-\frac{T}{Ta_1}\right)$

RESULTS AND DISCUSSION

RAS were carried out for the MASTeR test article on adapted unstructured grids to evaluate the ability of the adaptation to capture relevant high-speed reacting flow physics, and to characterize operating envelope. The unstructured grids were obtained using the adaptation tool with the Mach number as the adaptation sensor on which the adaptation error estimates were based. Since the experience with this tool is fairly new, the level of grid resolution required to achieve results comparable to those from structured simulations was unknown.

Plots of the one-dimensional mixing efficiency, one-dimensional combustion efficiency and Mach number contour plots on the streamwise plane through the centerline of injector ports are used in this analysis. The first grid generated using the adaptive grid tool is typically very coarse, but it does help to establish bulk inviscid structures and error estimates near the surfaces for boundary layer clustering in subsequent grids. All subsequent grids are generated using the solution from the previous grid simulation, with more information learned about the flowfield upon each adaptation. Figure 6 shows the grid and solution progression at the upstream shock location. The plots show Mach number contours, which is also the adaptation sensor field. The adaptive grid tool was run for 10 adaptation cycles, with the 10th adaptation representing the final solution. This location best shows the grid adaptation as the Mach number differences are greatest in this location. The Mach gradients downstream of the shock are less severe and although the adaptation is still taking place it is more difficult to visualize. The first grid created is very coarse and the grid cells are large in the boundary layer. However, the corresponding Mach number contours show near-wall gradients being introduced. These gradients prompt the adaptive grid tool to cluster the grid cells in those areas. At grid two, the boundary layer and stronger shocks have been identified and are being refined; more grid cells are being placed along the upstream shock, as well as the boundary layer. The interacting shocks that

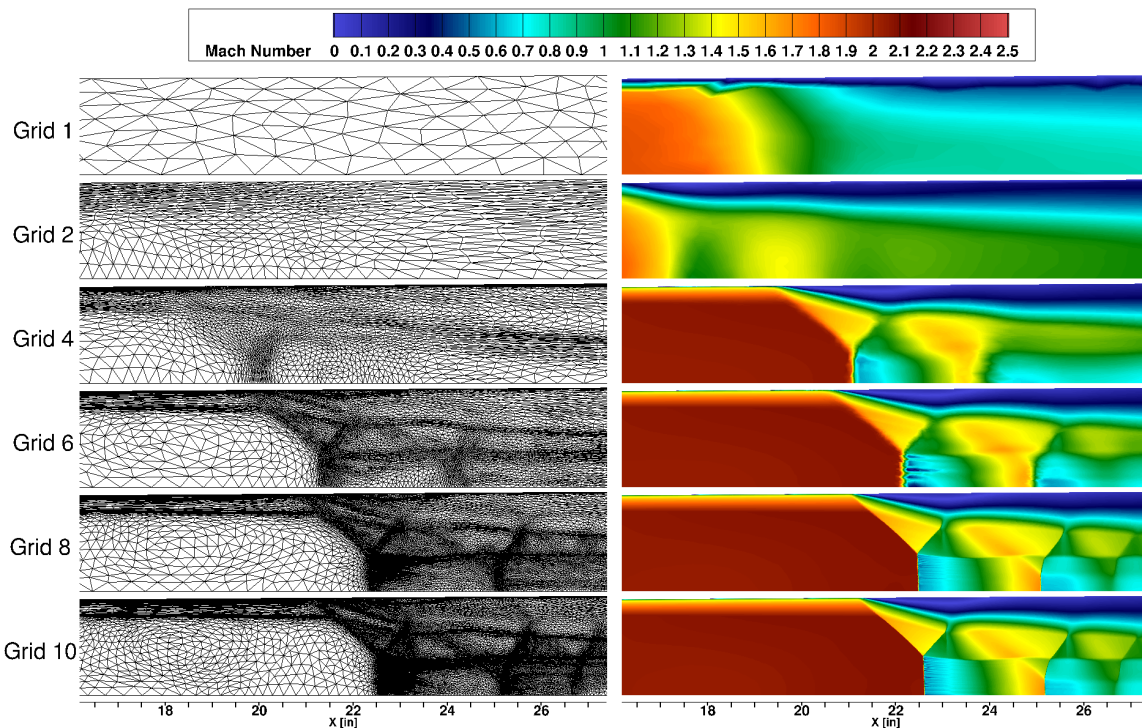


Figure 6. Grid progression (left) and Mach number contour solution progression (right) on the streamwise plane through the centerline of primary and secondary injector port.

occur downstream of the normal shock however, are not yet being resolved at this point. This is because these solutions use first-order numerics, which are dissipative. It should be noted that the Hessian-based error estimate assumes the solution was obtained with second-order numerics. Despite using first-order numerics, the error estimate is still able to drive adaptation for the first few adaptation iterations.

The significant change from grid 2 to grid 4 can be attributed to the grid doubling in complexity and the use of second order numerics. By grid 4, the normal shock and interacting downstream shocks begin to form and begin to be refined, allowing these features to be captured more clearly. By grid 6, the position of the normal shock begins to stabilize, and the interacting downstream shocks are being resolved. Many of the flow features have been found by the adaptive mesh tool at this point. All grids after this point work to further refine the features that have been identified. Further error reduction is achieved by increasing cell density around the flow features until all features appear to be well resolved in the final adaption.

When using the adaptive grid tool, the solution is determined to be grid-resolved when the change in the metric of interest becomes insignificant “enough” (as determined by the user) between select adaptation cycles. The adaptation cycles chosen for comparison in the grid convergence study depend on the user’s preference. For this work, adaptations for which the grid completed a stride, i.e., the grid points are only re-positioned, are compared.

The metrics of interest for the current work are the mixing efficiency and combustion efficiency. Plots of the mixing efficiency and combustion efficiency along the downstream distance for an ER1 of 0.38 and ER2 of 0.112 can be found in Figs. 7 and 8. All plots only display the mixing efficiency and combustion efficiency for the cavity region, as the mixing efficiency quickly reaches 1 downstream of the cavity and the fuel injectors are intended to fuel only the cavity. The results of grids 2 and 4 are not shown because the ignition sub-domain was present, which affects the underlying equations. The curves presented for these cases are representative of all others. A clear general trend can be seen from these figures; the mixing efficiency

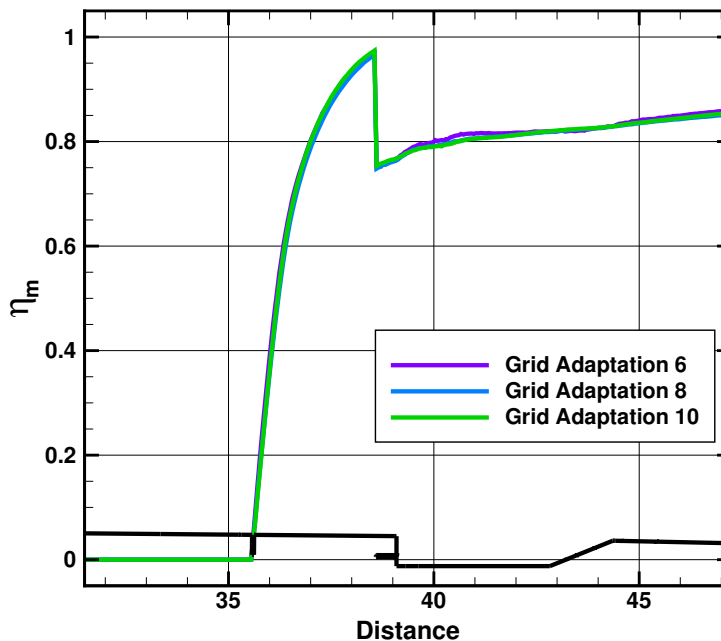


Figure 7. Mixing efficiency vs downstream distance (in inches) of the cavity region with a cavity L/D of 6, ER1 = 0.38, and ER2 = 0.112.

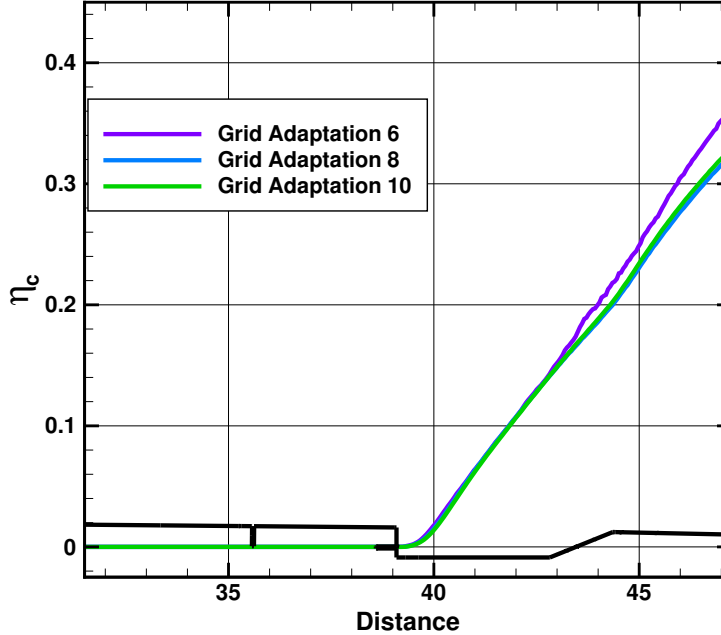


Figure 8. Combustion efficiency vs downstream distance (in inches) of the cavity region with a cavity L/D of 6.

is highest for the coarsest grids and becomes lower and lower as the grids are refined. This is expected, as the coarser grids exhibit more numerical dissipation, leading to higher mixing efficiency values on these grids. For all grid adaptations, the fuel from the primary injectors rapidly mixes until the start of the cavity. At this point more fuel is injected through the secondary injectors, resulting in a drop in mixing efficiency. The fuel continues to mix as it travels downstream, however, at a less rapid rate. The small differences of the mixing efficiency curves between grids 8 and 10 indicate that the grid adaptation method found a grid resolved solution, at least in terms of these metrics.

Figure 8 shows that combustion does not occur until the fuel reaches the cavity, even though fuel is being injected upstream by the primary injector. The fuel in the earlier grid adaptation also combusts at a higher rate further down the cavity than the later grid adaptations. This occurs due to more numerical dissipation when using the coarser grid. The small differences of the combustion efficiency curves between grids 8 and 10 indicate that the grid adaptation method found a resolved solution, at least in terms of these metrics.

Figure 9 shows the ER contour of the two symmetry planes of the cavity region for a case with primarily upstream fuel injection. For both symmetry planes, most of the fuel injected by the upstream primary injector travels along the wall and is entrained into the cavity, fueling the cavity uniformly and a portion of it makes its way into the core flow. Fuel from the secondary cavity injector stays closer to the cavity backward face. The secondary injector does not fuel the cavity as uniformly as the primary injector, as the fuel advection does not equally distribute the fuel. This can be seen when comparing the high ER regions close to the cavity backward face between the symmetry planes through the center of the secondary injector (top) and the symmetry plane in between the secondary injectors (bottom.)

Figure 10 shows the static temperature contour of the two symmetry planes of the cavity region for a case with primarily upstream fuel injection. Both symmetry planes indicate that burning of the fuel only occurs inside of the cavity. Fuel from the upstream injector does not ignite until it travels into the cavity. The cold

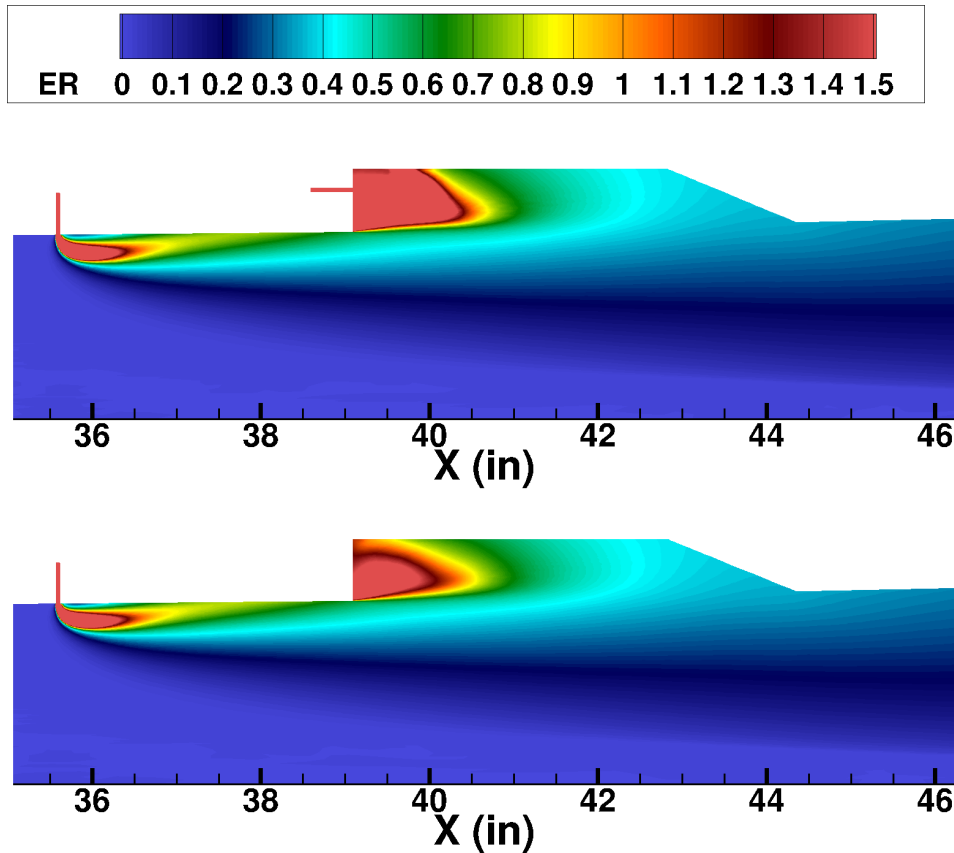


Figure 9. Cavity ER contours on streamwise plane through secondary injectors (top) and on streamwise plane between secondary injectors (bottom) for a cavity of L/D of 6, ER1 = 0.208, and ER2 = 0.01.

fuel from the secondary cavity injector does not ignite immediately and needs a rise in temperature from the surrounding air to start burning. This can be seen when looking at the symmetry plane through the center of the secondary injector (top.)

Figures 11, 12, 13, 14, and 15 show scatter plots of the correlations between the independent variables, ER1 and ER2, and the metrics of interest. A random scatter indicates there is a lack of correlation, whereas a trend would indicate a correlation. Figure 11 shows a scatter plot of the total ER versus local cavity ER (probed at 1.5 inches away from the cavity face and 0.1 inches away from the cavity floor at the midplane between secondary cavity injectors), combustion efficiency at the combustor exit, and leading shock train location. There is a strong correlation between total ER and the leading shock train location. As the total ER is increased the location of the shock travels farther upstream (toward zero). When the total ER is higher, there is more fuel both injected and burned, which increases the pressure of the cavity and leads to a farther upstream shock train location. There is only a weak correlation between the total ER and the local cavity ER. This is because, while the entirety of the fuel injected into the cavity (ER2) increases the local ER, only a portion of the fuel injected upstream (ER1) is entrained into the cavity and a portion bypasses the cavity. There is also a pronounced correlation between the local cavity ER and the combustion efficiency at the exit of the combustor. As more fuel is present in the cavity, the combustion efficiency at the combustor exit increases. This indicates that even for very high values of the local cavity ER, the preheating of the rich mixture of fuel and combustion products enhances the combustion process downstream of the cavity

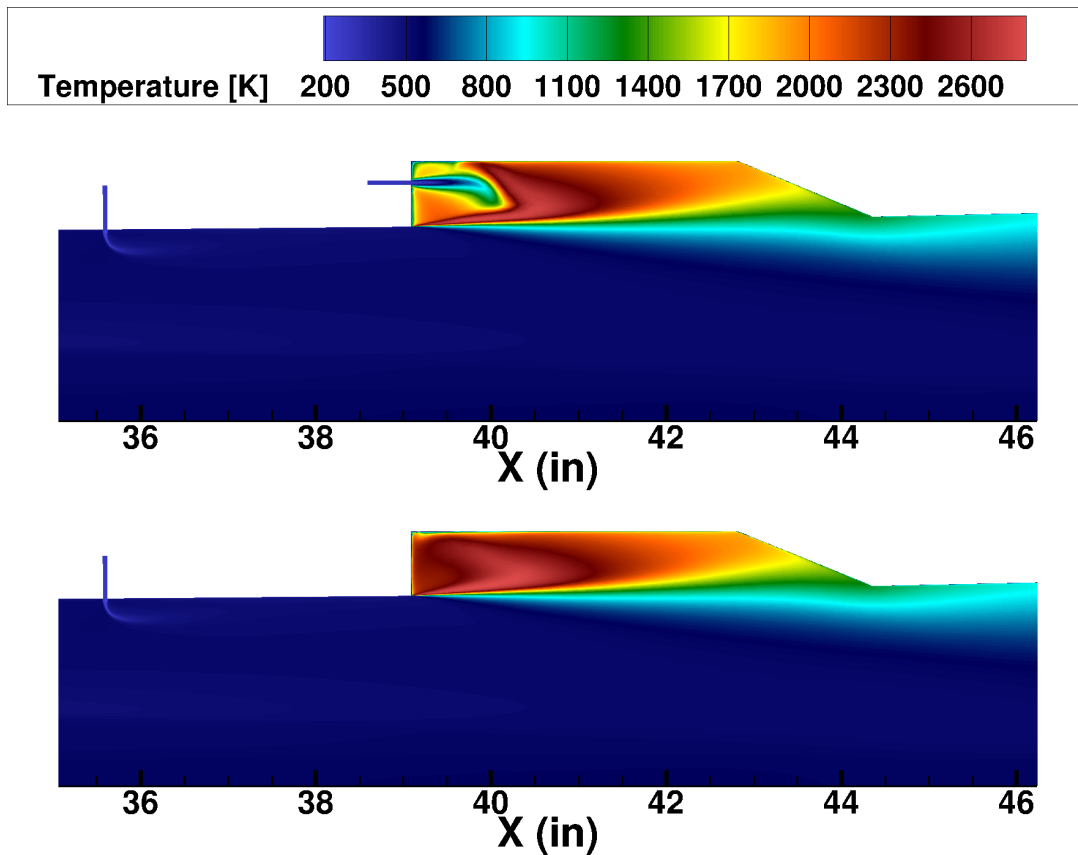


Figure 10. Cavity temperature contours on streamwise plane through secondary injectors (top) and on streamwise plane between secondary injectors (bottom) for a cavity of L/D of 6, $ER_1 = 0.208$, and $ER_2 = 0.01$.

when mixed with the fuel and air that bypassed the cavity. As expected, there is also a correlation between combustion efficiency and shock train location. As the combustion efficiency increases the shock moves upstream (toward zero). However, depending on the fuel injection distribution (ER_1 vs ER_2) it is possible to find configurations with high combustion efficiency yet downstream shock locations. These configurations are typically also associated with low total ER levels.

Figure 12 shows a scatter plot of ER_1 and ER_2 versus local cavity ER at various locations in the cavity, where the data is probed at the midplane between secondary cavity injectors. There are no clear correlations between ER_1 and any local cavity ER . This indicates that the amount of fuel injected upstream that enters the cavity does not significantly change with increasing ER_1 . However, there is a correlation between the secondary injection, ER_2 , and the local cavity ER for all locations. This is not surprising because injecting fuel directly into the cavity will increase cavity ER . Furthermore, all local ER values are also well correlated with each other. This is an indicator of how uniformly the fuel and air are mixed in the cavity. Linear correlation between pairs of cavity ER probes at various locations indicate the same value of ER and therefore the same mixture. Based on this reasoning, the $L/D=4$ cavity (denoted by green markers) appears to produce the most uniform mixtures in the cavity. When looking at only one L/D (i.e., just green, blue, or magenta), there is also a strong correlation. The strength of the correlations increase the farther downstream the local ER value is probed, i.e., the clustering of the points about a trendline is well defined. This is due to the fuel mixing more the farther downstream it travels.

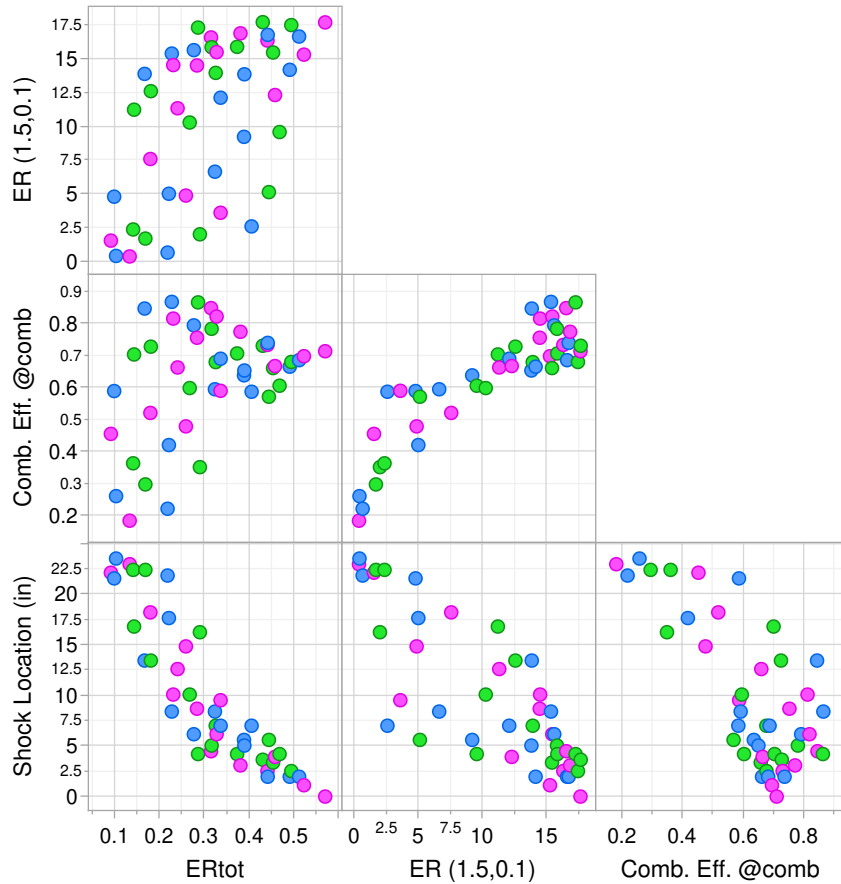


Figure 11. Scatter plot of total ER versus local cavity ER at a point 1.5 inches downstream of the cavity backward face and 0.1 inches above the cavity floor (1.5,0.1), combustion efficiency at the combustor exit, and leading shock train location, where 0 is the start of the isolator. The colors green, blue, and magenta denote the L/D values of 4, 6, and 8, respectively.

Figure 13 shows a scatter plot of ER1 and ER2 versus the local static temperature values at various locations in the cavity, where data is probed at the midplane between the secondary cavity injectors. The static temperatures are somewhat independent of ER1, but a flamelet-like correlation emerges for ER2, especially for the two near-wall (i.e., 0.1) probe locations. The flamelet-like correlation is characterized by a peak temperature near stoichiometric cavity ER, and decreasing values of temperature toward increasingly lean and rich values. For the other probe locations, this flamelet-like correlation between static temperature and ER2 can be observed for the individual values of cavity L/D, however, this is somewhat obfuscated by the combined scatter plot. Similar to the ERs at various locations, the static temperatures are also well correlated at various locations. Because the scatter plot is organized in order of upstream to downstream probes, these correlations emerge as vertical clusters that “tilt” toward linear correlation as the data is compared with the downstream probes, with the most linear correlation observed for the (3L/4,D/2) and (L/2,D/2) pair.

Figure 14 shows a scatter plot of ER1 and ER2 versus local mass fraction of water at various locations in the cavity, where data is probed at the midplane between the secondary cavity injectors. The mass fraction of water can be used to determine at which locations the fuel is being burned as it is a product of the reaction, although, fuel can be burned at a different location and water can be advected to other locations. The character of correlations between ER1 and ER2, and water mass fraction is comparable to that found for the temperature. For all locations, the mass fraction of water tends to approach similar values regardless of

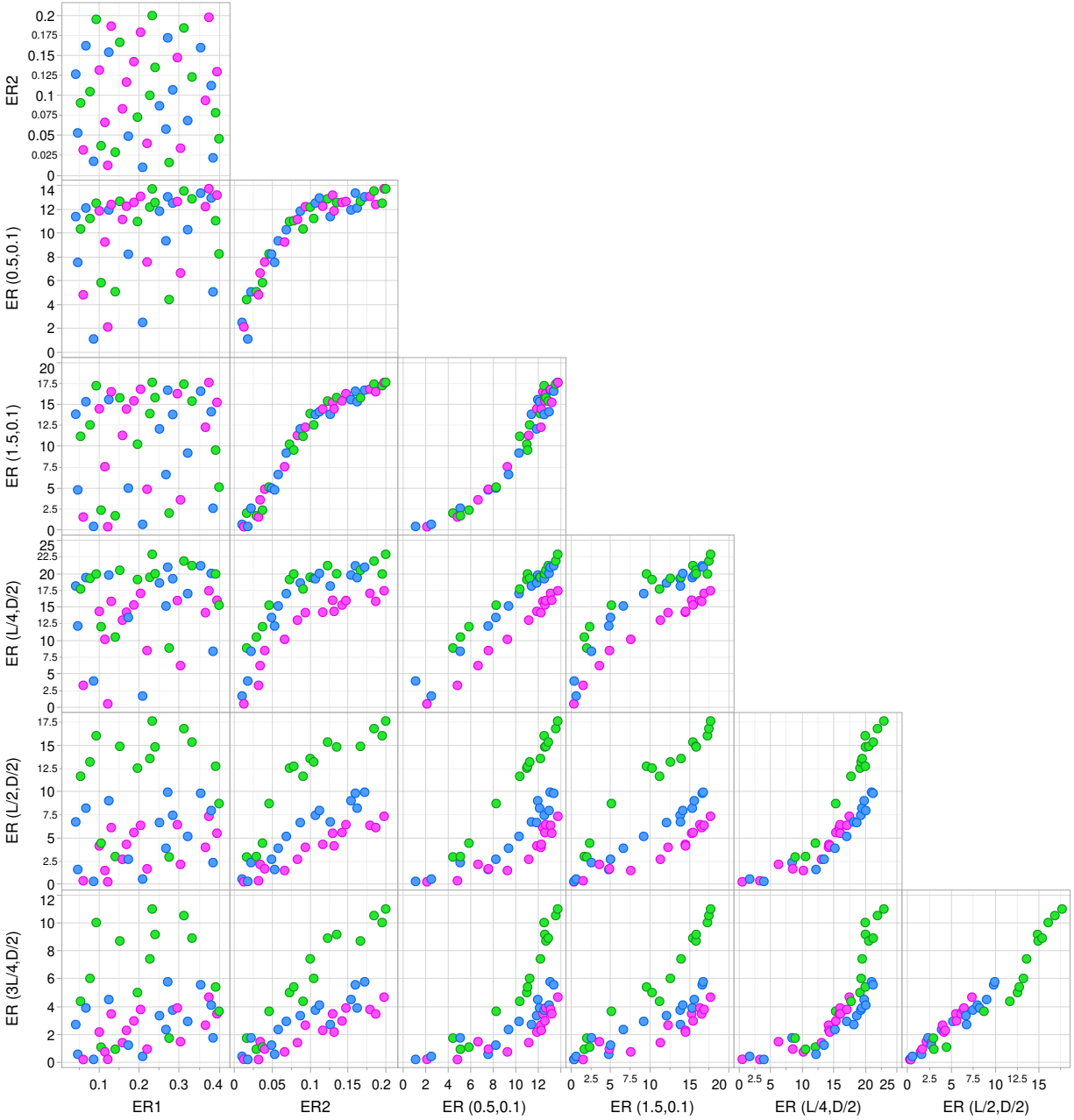


Figure 12. Scatter plot of ER1 and ER2 versus local ER values at various locations in the cavity. Data probed at the midplane between secondary cavity injectors. The colors green, blue, and magenta denote the L/D values of 4, 6, and 8, respectively.

ER1. However, there are several cases, which correspond to very lean overall and lean in-cavity conditions, for which the water mass fraction is below the group clustering, more so for the downstream probe locations. This could indicate that the local ER in the cavity could be approaching the local extinction limit and that water is being advected to those locations before diffusing out of the cavity. For ER2, the clustering of points once again follows a flamelet-like characteristics with peak water mass fraction around stoichiometry and decreasing values away from it. This is particularly pronounced for near-wall probe locations. Consistent with correlations observed for the static temperatures, the water mass fractions are also well correlated

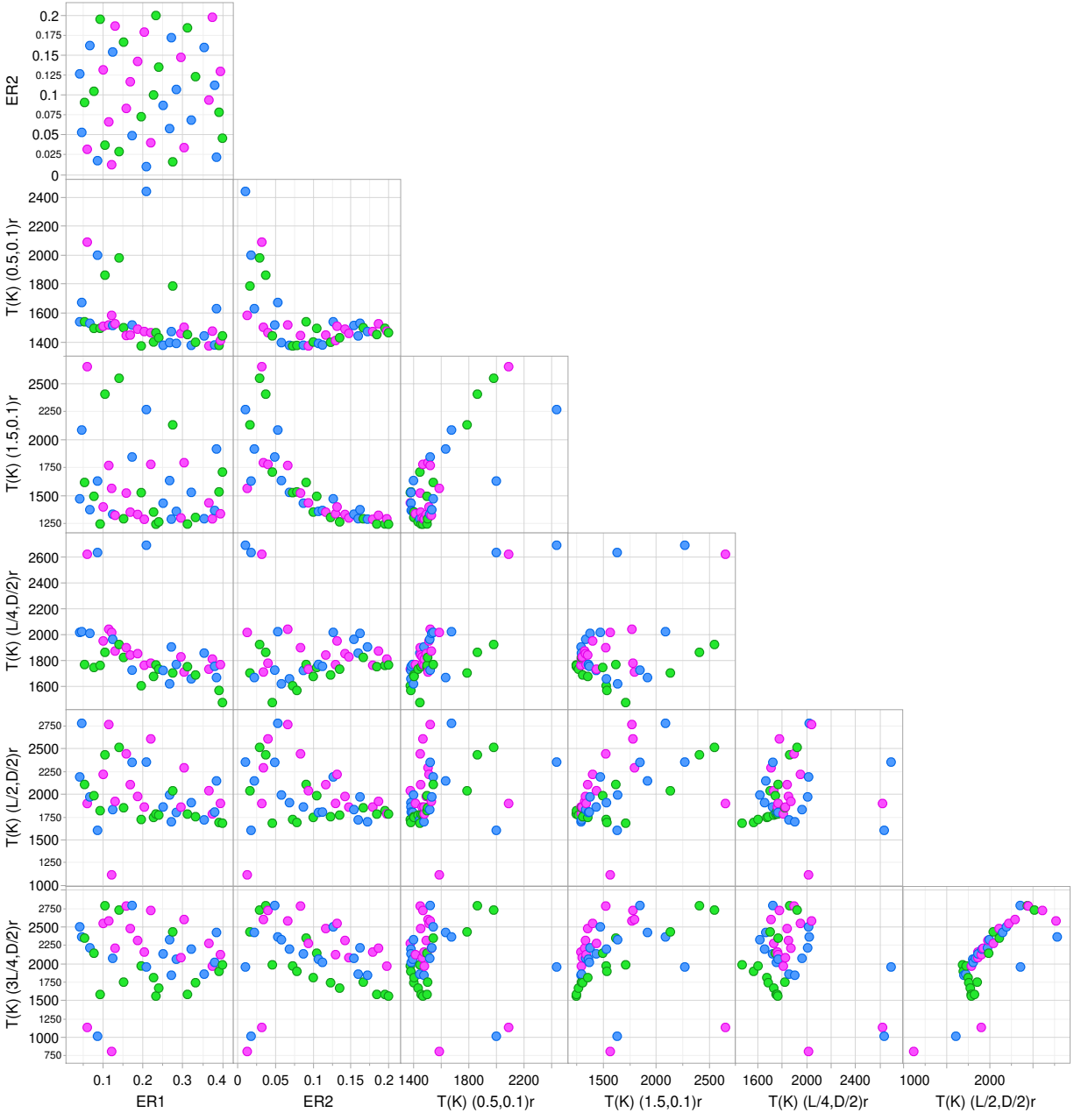


Figure 13. Scatter plot of ER1 and ER2 versus local static temperature values at various locations in the cavity. Data probed at the midplane between secondary cavity injectors. The colors green, blue, and magenta denote the L/D values of 4, 6, and 8, respectively.

with each other at various locations except for the few outlier cases. These correlations emerge as vertical clusters that turn toward linear correlation as the ER values increase.

Figure 15 is a compilation of the previous scatter plots containing scatter of ER1 and ER2, and ER, static temperature, and water mass fraction at (1.5,0.1) location, and mixing and combustion efficiency at the end of the cavity. This scatter plot indicates a fairly weak correlation between ER1 and other quantities with the exception of combustion efficiency. Across all values of L/D, as ER1 increases the combustion efficiency

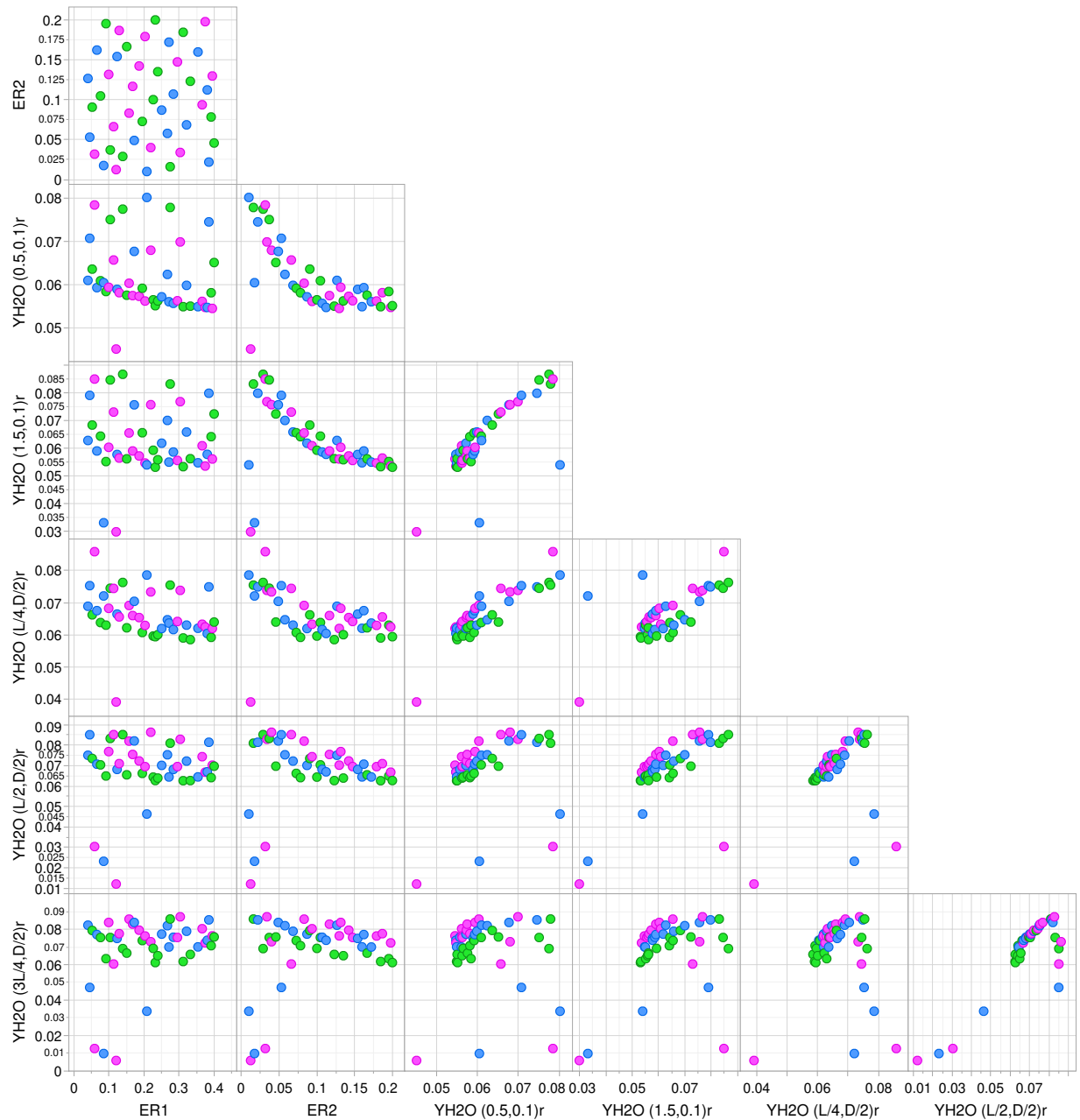


Figure 14. Scatter plot of ER1 and ER2 versus local mass fraction of water at various locations in the cavity. Data probed at the midplane between secondary cavity injectors. The colors green, blue, and magenta denote the L/D values of 4, 6, and 8, respectively.

decreases. This is not necessarily a surprise for this case because as ER1 increases the fuel penetration also increases resulting in more fuel penetrating into the core flow and further away from the cavity shear layer. Therefore, about the same amount of fuel injected upstream is entrained into the cavity independently of ER1. Because of this, also about the same amount of hot combustion product and radicals are ejected from the cavity into the core flow; therefore, a proportionally larger fraction of the mixture remains unburned as measured at the exit of the cavity. It should be noted that for many of the lower ER1 values, the mixing

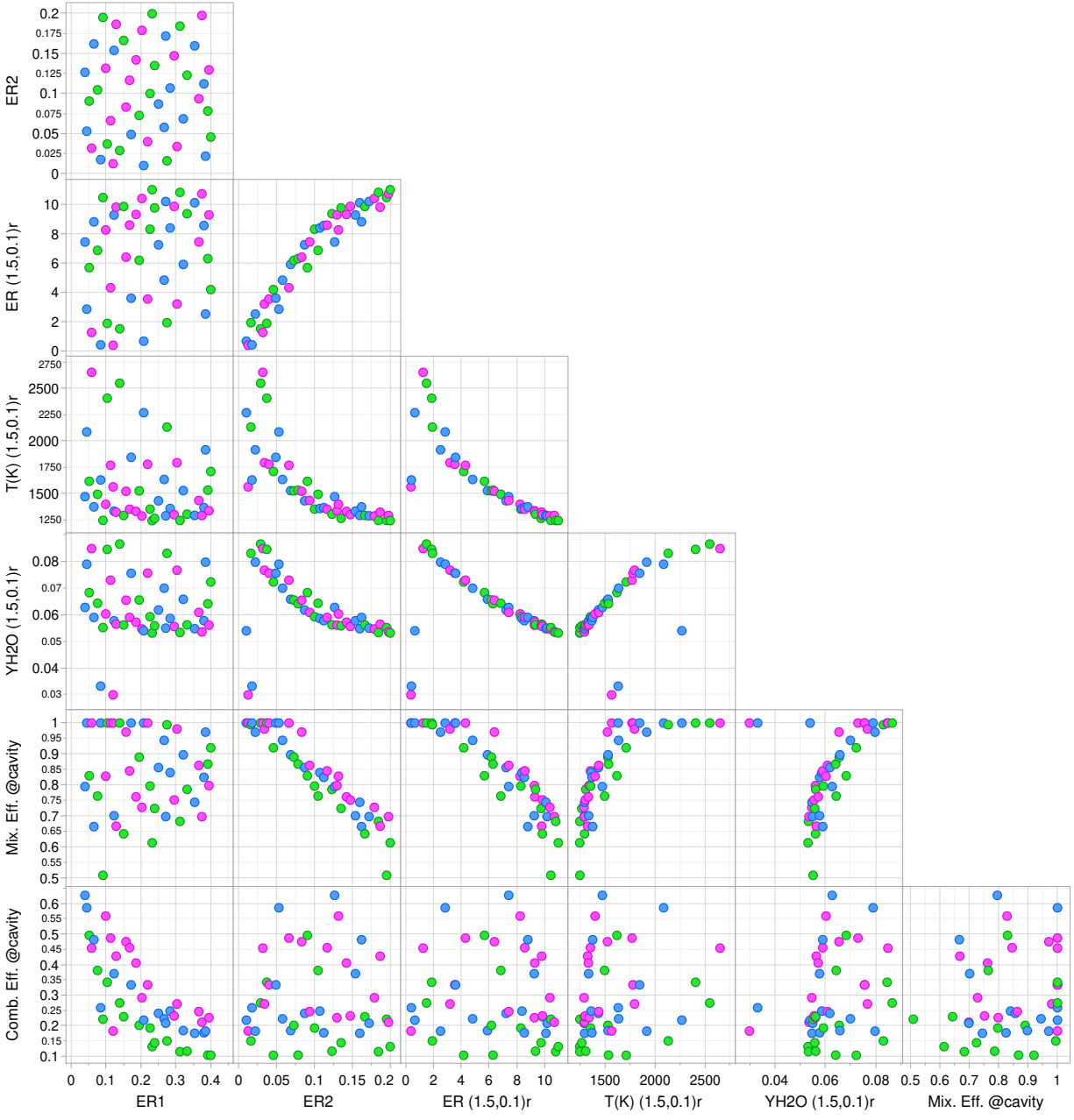


Figure 15. Scatter plot of ER1 and ER2 versus local ER, temperature, mass fraction of water, and mixing and combustion efficiencies at various locations in the cavity. Data probed at the midplane between secondary cavity injectors. The colors green, blue, and magenta denote the L/D values of 4, 6, and 8, respectively.

efficiency reaches one by the end of the cavity. This is due to less fuel needing to be mixed with the surrounding air than the higher ER cases, so a potentially reactable distribution is achieved faster.

As discussed before, there is a correlation between ER2 and the local ER, static temperature, and water mass fraction. There is also a correlation between ER2 and the mixing efficiency. As ER2 increases, the global mixing efficiency measured at the cavity exit decreases. This is expected because fuel injected into

the cavity is effectively separated by the cavity shear layer from the core flow air with which it can mix. The lower ER2 values also have a tendency to reach one by the end of the cavity as was the case for ER1. However, there is no correlation between ER2 and the combustion efficiency at the end of the cavity. This indicates that combustion processes in the cavity are decoupled from those of the core flow. However, as demonstrated in Figure 11, the preheating of the rich mixture of fuel and combustion products enhances the combustion process downstream of the cavity when mixed with the fuel and air that bypasses the cavity.

SUMMARY AND CONCLUSIONS

The application of an automated unstructured grid adaptation tool to simulations of high-speed fuel injection and reacting physics was investigated using RAS. The flowfield studied occurs in the MASTeR test article with a Mach 2 facility nozzle and three cavity length-to-depth (L/D) ratios of 4, 6, and 8. This investigation was carried out to provide an understanding about the MASTeR operating conditions in the experimental space. A Latin hypercube sampling method was used to generate a design-space-filling list of cases to simulate, totaling in 45 cases, with the primary (ER1), secondary (ER2) injection equivalence ratios, and cavity length-to-depth ratio as the independent variables.

The results of this investigation provided knowledge of the operating performance of the MASTeR. The correlations between the independent variables, ER1 and ER2, and the metrics of interest: mixing efficiency, combustion efficiency, local ER, and isolator shock train location, were determined. It was found that the cavity operated somewhat independently of the core flow, however, there was a positive correlation between the combustor efficiency at the combustor exit and a local ER measured inside the cavity. The total injected ER also correlated well with the shock train upstream position. Surprisingly, the local cavity ER was not correlated with the amount of fuel injected upstream of the cavity (ER1). This indicated that about the same amount of fuel was entrained into the cavity via transport through the cavity shear layer regardless of the value of ER1.

Future work will include other parameters that impact the operation of the MASTeR, such as, additional cavity depths, other fuels, various Mach number facility air flow conditions, and total temperature conditions. Additional metrics of interest will also be considered. Those may include cavity residence time and mass entrainment rate.

ACKNOWLEDGMENTS

This work is supported by the Hypersonic Technology Project (HTP) in the Advanced Air Vehicles Program (AAVP) of the NASA Aeronautics Research Mission Directorate (ARMD). Computational resources are provided by the NASA Langley Research Center and the NASA Advanced Supercomputing (NAS) Division.

REFERENCES

- [1] Ben-Yakar, A. and Hanson, R. K., ***Cavity Flame-Holders for Ignition and Flame Stabilization in Scramjets: An Overview***, J. Propul. Power, 17(4):896–877 (2001).
- [2] Cai, Z., Wang, T., and Sun, M., ***Review of Cavity Ignition in Supersonic Flows***, Acta Astronaut, 165:268–286 (2019).
- [3] Liu, Q., Baccarella, D., and Lee, T., ***Review of Combustion Stabilization for Hypersonic Airbreathing Propulsion***, Prog. Aerosp. Sci., 119 (2020).

- [4] Choubey, G., Devarajan, Y., Huang, W., Mehar, K., Tiwari, M., and Pandey, K., **Recent Advances in Cavity-Based Scramjet Engine: A Brief Review**, *Int. J. Hydrog. Energy*, 44:13895–13909 (2019).
- [5] Hassan, E. A., Ombrello, T., and Peterson, D. M., **Ignition and Flame Propagation in Cavity-Fueled Supersonic Flameholder**, in *AIAA Scitech Forum*, San Diego, CA (2019).
- [6] Ombrello, T., Turner, A., and Salupo, S., **Axi-Modular Cavity Rig**, Tech. Rep. ISSI-F003-21, Air Force Research Laboratory (2022).
- [7] Riggins, D. W., McClinton, C. R., and Vitt, P. H., **Thrust Losses in Hypersonic Engines Part 1: Methodology**, *J. Propul. Power.*, 13(2):281–287 (1997).
- [8] Mao, M., Riggins, D. W., and McClinton, C. R., **Numerical Simulation of Transverse Fuel Injection**, in *Computational Fluid Dynamics Symposium on Aeropropulsion*, NASA-CP-3078, pages 635–667, NASA, Cleveland, OH (Apr. 1990).
- [9] **Scramjet Propulsion Testing Recommended Practices and Guidelines**, Chemical Propulsion Information Agency, 2 edn. (Mar. 2005).
- [10] VULCAN-CFD, <http://vulcan-cfd.larc.nasa.gov/> (2023).
- [11] Kleb, B., Park, M. A., Wood, W. A., Bibb, K. L., and Thompson, K. B., **Sketch-to-Solution: An Exploration of Viscous CFD with Automatic Grids**, in *AIAA Aviation Forum*, AIAA 2019-2948, AIAA, Dallas, TX (Jun. 2019).
- [12] O’Connell, M., White, J., and Thompson, K. B., **Towards an Automated Unstructured Grid Adaptation Workflow with VULCAN**, in *AIAA Aviation Forum*, AIAA 2021-2701, AIAA, Virtual (Aug. 2021).
- [13] Haimes, R. and Dannenhoffer, J. F., III, **The Engineering Sketch Pad: A Solid-Modeling, Feature-Based, Web-Enabled System for Building Parametric Geometry**, in *21st AIAA Computational Fluid Dynamics Conference*, AIAA 2013-3073, AIAA, San Diego, CA (Jun. 2013).
- [14] Haimes, R. and Drela, M., **On The Construction of Aircraft Conceptual Geometry for High-Fidelity Analysis and Design**, in *50th AIAA Aerospace Sciences Meeting*, AIAA 2012-683, AIAA, Nashville, TN (Jan. 2012).
- [15] Park, M. A., **Anisotropic Output-Based Adaptation with Tetrahedral Cut Cells for Compressible Flows**, Ph.D. thesis, Massachusetts Institute of Technology, Boston, MA (Sep. 2008).
- [16] Si, H., **TetGen, a Delaunay-Based Quality Tetrahedral Mesh Generator**, *ACM Transactions on Mathematical Software (TOMS)*, 41(2):11:1–11:36 (2015).
- [17] van Leer, B., **Towards the Ultimate Conservative Difference Scheme. V: A Second-Order Sequel to Godunov’s Method**, *J. Comput. Phys.*, 32(1):101–136 (Jul. 1979).
- [18] Edwards, J. R., **A Low-Diffusion Flux-Splitting Scheme for Navier-Stokes Calculations**, *Comput. Fluids.*, 26(6):635–659 (Jul. 1997).
- [19] McBride, B. J., Gordon, S., and Reno, M. A., **Thermodynamic Data for Fifty Reference Elements**, NASA Technical Paper 3287/REV1, NASA, Cleveland, OH (Feb. 2001).
- [20] White, J. A., Baurle, R. A., Passe, B. J., Spiegel, S. C., and Nishikawa, H., **Geometrically Flexible and Efficient Flow Analysis of High Speed Vehicles Via Domain Decomposition, Part 1, Unstructured-grid Solver for High Speed Flows**, in *JANNAF Meeting / 48th CS / 36th APS / 36th EPSS / 30th PSHS Joint Subcommittee Meeting* (Dec. 2017).
- [21] Menter, F. R., **Two-Equation Eddy-Viscosity Turbulence Models for Engineering Applications**, *AIAA J.*, 32(8):1598–1605 (Aug. 1994).
- [22] Wilcox, D. C., **Turbulence Modeling for CFD**, DCW Industries, Inc., La Cañada, CA (2006).